# How Beam Damage Can Skew Synchrotron Operando Studies of Batteries

Thibaut Jousseaume, Jean-François Colin, Marion Chandesris, Sandrine Lyonnard, Samuel Tardif

ACS Energy LETTERS

http://pubs.acs.org/journal/aelccp

# How Beam Damage Can Skew Synchrotron *Operando* Studies of Batteries

Thibaut Jousseaume, Jean-François Colin, Marion Chandesris, Sandrine Lyonnard, and Samuel Tardif*

Cite This: *ACS Energy Lett.* 2023, 8, 3323−3329 Read Online

ACCESS | Metrics & More | Article Recommendations | Supporting Information

**ABSTRACT:** With the advent of high-brilliance synchrotron sources, the issue of beam damage on the samples deserves proper attention. It is especially true for *operando* studies in batteries, since the intense photon fluxes are commonly used to probe ever finer effects. Here we report on the causes and consequences of synchrotron X-ray beam damage in batteries, based on the case study of *operando* X-ray diffraction. We show that beam damage is caused by the mingled actions of dose and dose rate. The aftereffects can lie in a broad range, from mild modifications of the crystalline structure to artificial phase transitions, and can thus impede or bias the understanding of the mechanisms at play. We estimate the doses at which the different effects appear in two materials, suggesting that it could be expanded to other materials with the same technology. We also provide recommendations for the design of *operando* synchrotron experiments.

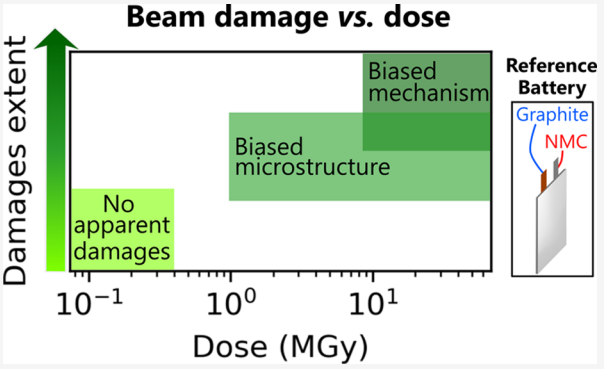




*Operando* experiments in batteries have offered valuable insights into the mechanisms at play inside the devices and thus have been performed using a variety of probes, e.g. neutrons, photons (from visible light to X-rays), electrons, and acoustic or nuclear magnetic resonance.[1−8] In particular, synchrotron radiation techniques such as spectroscopy, imaging, or diffraction offer a good penetration depth, element selectivity, and a large sensitivity that enable fast acquisitions, taking advantage of the intense photon flux available. The downside of using a large incident photon flux is the increase of unwanted interactions of the X-rays with the sample under scrutiny. In batteries, photoabsorption and Compton scattering by the different components of the electrochemical cell (active or inactive materials) can result in deleterious side effects, ultimately leading to the rapid degradation of the device. This so-called "beam damage" has already been clearly identified in several scientific fields,[9,10] including structural biology, where the radiation dose during a protein crystallography experiment has been closely monitored.[11−13] Yet, only a few studies have been dedicated to the effect of the X-ray beam on the behavior of battery materials,[14−19] and while the possibility of beam damage is usually acknowledged, clear guidelines to avoid it are still missing.

Here we endeavor to provide a quantitative analysis of the beam damage in archetypal liquid-based Li-ion batteries. The exact mechanisms of the beam damage are still elusive, probably quite numerous, and certainly dependent on the energy of the X-ray beam. We thus focus on evidencing the multiple possible effects of beam damage and the conditions for their onset, using *operando* synchrotron X-ray diffraction (S-XRD) in the hard X-ray regime (27 keV), a common technique to investigate the crystal structure of the active materials during cycling. We performed a series of three dedicated *operando* S-XRD experiments to evaluate beam-induced structural changes in standard graphite vs $LiNi_{0.6}Mn_{0.2}Co_{0.2}O_2$ (NMC622) or $LiNi_{0.8}Mn_{0.1}Co_{0.1}O_2$ (NMC811) pouch cells. Experiment 1 was designed to show how varying the X-ray exposure may induce a distinct typical structural evolution. In experiment 2, we irradiated different zones of the same pouch cell, with increasing exposure time: i.e., increasing dose. Finally, experiment 3 aimed at evaluating the dose rate effect using cells receiving a comparable integrated dose but over different lengths of time. Accordingly, we first discuss artificial phase transitions during cycling that are induced by high X-ray exposure. Then we report on more subtle effects on the crystal structure of the electrode materials at intermediate exposures. Finally we estimate the doses and

**Received:** April 19, 2023
**Accepted:** May 19, 2023

dose rates to provide quantitative threshold limits for the studied systems.

Two distinct lithium insertion (lithiation) mechanisms in the cathode material NMC622 have been reported in the literature, corresponding to two different lattice parameter evolutions.[20,21] The first model follows a solid-solution mechanism along the whole lithium stoichiometry range. It describes a single phase where the lattice parameters continuously change as the overall lithium content $c_{Li}$ is varied, which is characterized by diffraction peaks shifting continuously in reciprocal space. In contrast to this continuous evolution of the solid-solution, a phase transition mechanism presents the coexistence of at least two phases at a given $c_{Li}$, and it is the phases' relative weights that change with $c_{Li}$. For the second model, the material evolution swings between distinct solid-solution and phase transition ranges as the lithium is inserted or extracted, and accordingly the diffraction peaks are treated as either single peaks or multimodal peaks, respectively. We show that both behaviors can actually be observed in the same material within the same stoichiometry range, depending only on the measurement conditions and more particularly on the radiation dose.

In experiment 1, two pouch cells with similar graphite electrodes and NMC622 electrodes were prepared and charged at the same C/2 rate. The S-XRD was measured *operando* in transmission as the Li was removed from the NMC, using two measurement protocols. In pouch cell a (PCa), the radiation dose was spread over a large area of 2.25 $mm^2$ by moving the cell after each scan. In pouch cell b (PCb), the acquisitions were always performed on the very same spot of 0.12 $mm^2$ and the NMC electrode was 19 $\mu$m (54%) thicker than PCa. The higher photon flux ($8 \times 10^{10}$ vs $6 \times 10^{10}$ ph $s^{-1}$) and the larger amount of absorbing material resulted in a larger amount of radiation absorbed in PCb than in PCa. The respective evolution of the 113 Bragg reflection shown in Figure 1A,B describes both *a* and *c* lattice parameters of the NMC622 hexagonal lattice. The initial peak position and shape are the same, but their evolution is drastically different. In PCa, the shape of the diffraction peak is maintained while the peaks move continuously. On the contrary, in PCb, the peak hardly

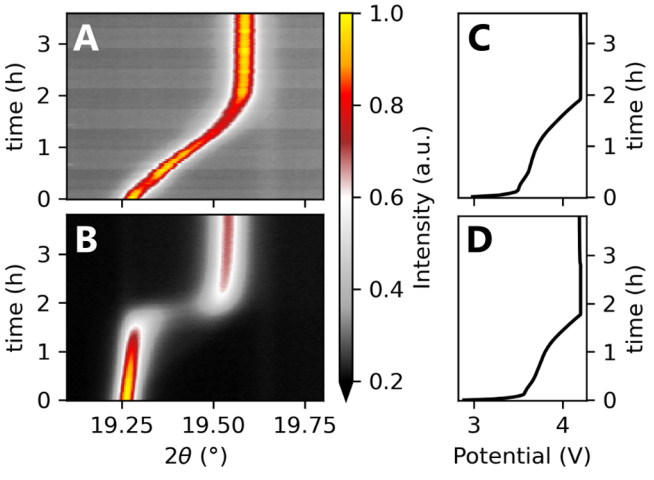


**Figure 1. Raw intensity of the 113 Bragg reflection of NMC622 while charging at C/2 with a 4.2 V hold whether the pouch cell has an X-ray dose (A) spread over 2.25 $mm^2$ or (B) focused on a single point (respectively PCa and PCb). (C, D) The respective potential curves.**

shifts at the beginning of the experiment, which could be interpreted as inactive material at that location. Then, after about 1.5 h of charging, its shape suddenly changes and splits into two peaks to become bimodal for a short period of time. During that time, the intensity of the initial peak decreases while that of the new peak increases, until only the latter remains and stays constant up to the end of the charge. Those two behaviors precisely describe the rival lithiation mechanisms reported in the literature: that is, either a solid-solution or a combined phase transition/solid-solution process. Thus, both mechanisms can be obtained, depending on whether the material is weakly or strongly irradiated.

Experiment 2 is set up to quantify more precisely the beam effect on batteries by successively moving between three locations increasingly exposed to X-rays, while measuring the *operando* S-XRD in an NMC811 vs a graphite cell sealed in pouch cell c (PCc) (Figure 2). A single detector image

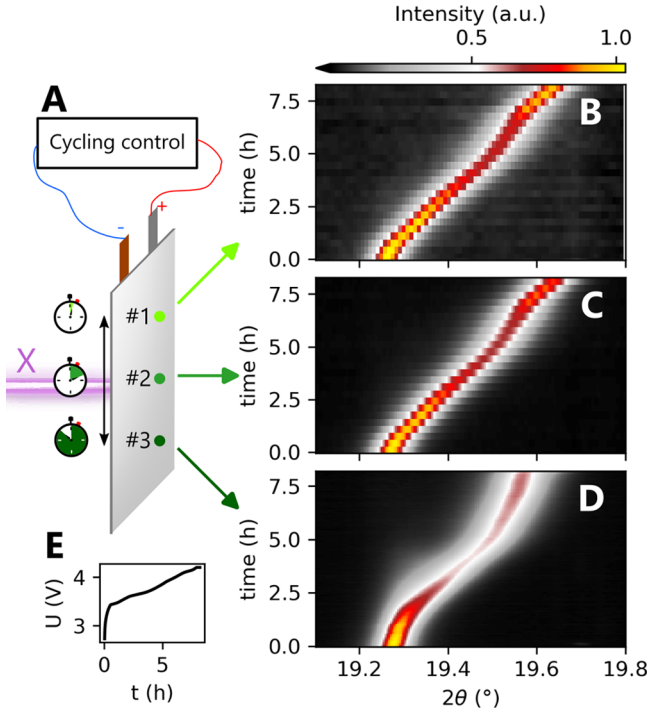


**Figure 2. (A) *Operando* S-XRD experimental setup designed to quantify the impact of exposure time, 2.5 s per scan at location #1, 98 s at #2 and 1050 s at #3. (B–D) Intensity color maps of the NMC811 113 Bragg reflection while pouch cell c is cycling at C/8 at locations #1, #2, and #3 respectively. (E) Cell potential.**

(limited *q* range) was taken at location #1, resulting in a total exposure of 2.5 s per measurement, including all motor movements. At location #2 (#3), a single (ten) $2\theta$ scan consisting in several detector images was taken, resulting in a total exposure of 98 s (1050 s) per measurement. Locations #1, #2, and #3 thus received different X-ray doses, proportional to their different exposure times.

The influence of the dose is first investigated by looking at the 113 Bragg reflection of NMC811, where there are no overlapping peaks from other cell materials, as shown in Figure 2. The initial and final XRD patterns of each location are compared in Figure 3A, where the intensities have been normalized to the initial peak amplitude. At the beginning of the electrochemical cycling, the peaks have very similar shapes



https://doi.org/10.1021/acsenergylett.3c00815
ACS Energy Lett. 2023, 8, 3323−3329

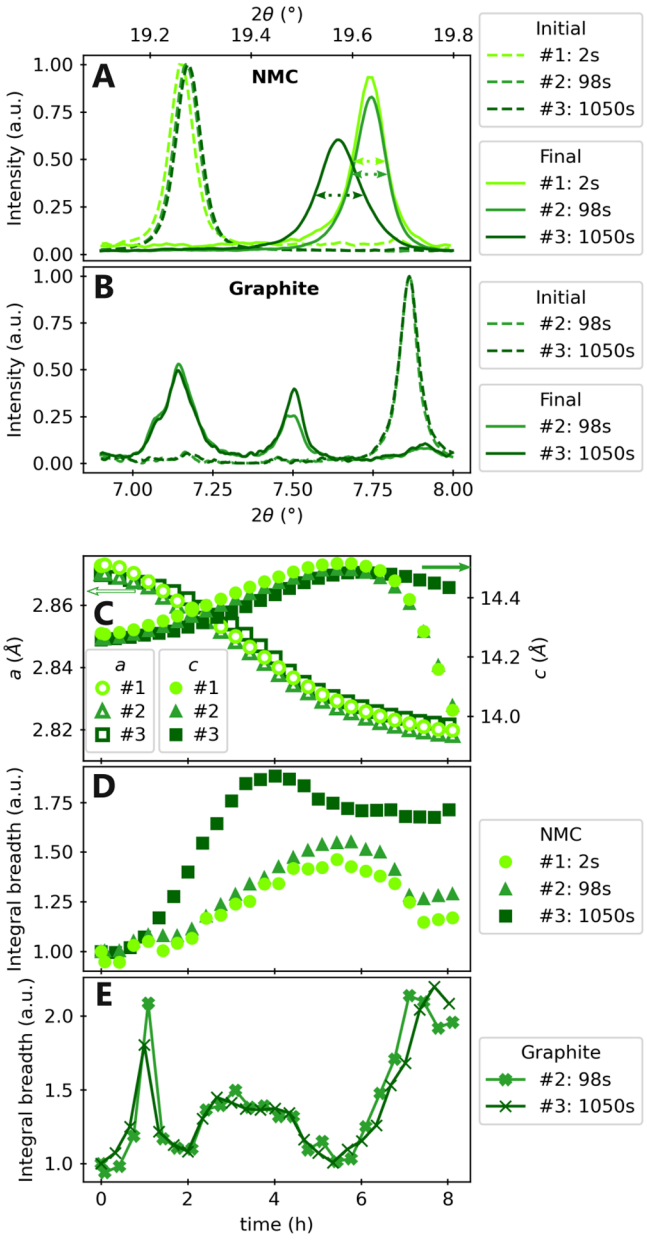


**Figure 3. (A) (respectively B) The first and last measurements of the 113 peak of NMC811 (respectively 002 peak of graphite and $LiC_{12}$ or 001 of $LiC_6$) performed at the three (respectively two) locations in PCc enduring different exposure times, and the final fwhms. The initial scattering in peak position is related to the nonexact simultaneity of measurements at a location while the cell is cycling. (C) *a* and *c* lattice parameters of NMC811 from a Le Bail refinement of patterns measured at the three locations and (D) integral breadth (IB) of the NMC 113 Bragg reflection normalized by the initial integral breadth as a function of time. IB is calculated in the [19.1°, 19.8°] range. Note that only a subset of all data points has been plotted for clarity; the whole set is shown in Figure S1. (E) Normalized IB of $Li_xC_6$ peaks in the [6.9°, 8°] range. The corresponding cell potential is shown in Figure S2.**

and intensities, indicating a homogeneous initial state, while at the end of charging, we observe a significant variation in shape and position depending on the dose received. At location #1, the peak shifts to a higher angle with an intensity comparable to that of the starting state, indicating that the same quantity of material reached the same final state. The 6.7% of difference can be attributed to a weak distribution of lattice parameters (Figure S3), i.e. a heterogeneous lithiation state, which has already been reported in NMC materials.[22−24] The peaks at locations #1 and #2 both reach 19.64°, while location #3 is limited to a smaller angle, indicating an impaired lithiation at that location. However, locations #2 and #3 both have smaller amplitudes and larger full widths at half-maximum (fwhms).

The evolution of the lattice parameters obtained from Le Bail refinements of the initial and final measurements at each location are reported in Table 1, using location #1 as the reference. They support an identical initial crystalline structure for the three locations, as already inferred from Figure 3A. However, after cycling, the pattern refinement at location #3 gives lattice parameters that are significantly different from those of the other locations, suggesting a modified evolution.

**Table 1. Lattice Parameter Differences from the Reference Location #1 (Å) from Le Bail Refinement of Initial and Last Scans Recorded at Locations Shot with Different X-ray Doses[a]**

| param | loc #1 | loc #2 | loc #3 |
|---|---|---|---|
| $a - a_0$ | 0 | −0.0016 | −0.0023 |
| $c - c_0$ | 0 | −0.023 | −0.025 |
| $a - a_f$ | 0 | −0.0018 | 0.0014 |
| $c - c_f$ | 0 | −0.009 | 0.423 |

[a]The parameters at reference location #1 are $a_0$ = 2.8723(8) Å and $c_0$ = 14.282(5) Å in the initial state and $a_f$ = 2.820(1) Å and $c_f$ = 14.01(2) Å in the final state.

The detailed evolution of the lattice parameters is shown in Figure 3C. While locations #1 and #2 follow the same evolution, typical of NMC materials, location #3 deviates from the common trend after about 1 h and the kinetics seems greatly impeded. Indeed, at the end of the 8 h charge, both the *a* and *c* values at location #3 correspond to those of locations #1 and #2 at 7 h, which indicates that the charge was only 88% complete at location #3. Therefore, it seems that the beam damage at the most exposed location resulted in lower local performances and an evolution of the lattice parameters that is not representative of unexposed materials. This decrease in reaction kinetics and its relation to the X-ray energy in the 15−35 keV range has been reported by Christensen et al. in various Li-ion chemistries.[17] While the impact of the large dose on the crystal evolution at location #3 is obvious, we show in the following that it can also have other subtle yet measurable effects at lower doses.

Location #2 seems to display a similar evolution of the crystal structure as location #1 (Table 1 and Figure 3C); however, the relative height of the 113 peak is different (Figure 3A). This indicates that such an intermediary dose can already impact the peak intensity. The beam effect during the cycling can also be seen in the evolution of the 113 peak width of NMC811 (Figure 3D). To measure the peak width, we used the integral breadth (IB) defined by IB = $(\int_\theta I\, d\theta)/\max(I)$, with *I* being the intensity. The IB is a measure of the peak width that does not rely on any assumptions or mathematical model of the peak shape. During the first few measurements, the peak width is the same for all the locations. Upon charging, the peak width starts to increase with the dose received: while the trend is similar for all locations, the broadening is more pronounced at location #2 after 4 h and even more at location


https://doi.org/10.1021/acsenergylett.3c00815
ACS Energy Lett. 2023, 8, 3323−3329

#3 after only 1 h. Those more subtle effects are probably due to a widening of the distribution of lithiation states being simultaneously probed by the X-ray beam and caused by a moderate increase of the electrical resistivity. This finding has a direct impact: even if the refinements of lattice parameters are not affected by relatively small X-ray doses, the irradiation can impact the analysis of the peak broadening and impair the estimations of isotropic strain and of the nature and position of atoms from Le Bail or Rietveld refinements that depend on it.

The use of a full cell and wider angular scans at locations #2 and #3 allows us to probe the graphite behavior as well. The graphite evolution does not seem impacted by the dose, except at the end of the charge, where the evolution of the IB of location #3 seems to be slightly lagging behind that of location #2 (Figure 3BE and Figures S6 and S7). The calculation of the phase fractions of $LiC_{12}$ and $LiC_6$ also suggests that the evolution of the composition at the high dose location is late at the very end of charging (Figure S8). This could be due to either the direct beam damage in the graphite electrode or the reduction in the kinetics of the damaged communicating cathode area, which is discussed in the following.

Moreover, we show that the beam may not only bias crystal structure refinements but also can entirely hinder the recorded delithiation (or lithiation) behavior because it skews the peak evolution. Looking in detail at the NMC 003 reflection in the initial state and after 3 h at C/8 suggests that no phase transition is taking place at the moderately irradiated location #2, whereas two peaks can be seen at the strongly irradiated location #3 (Figure 4A,B). The weaker peak vanishes during the charge (Figure S4) and could be wrongly interpreted as a phase transition, likely due to the coexistence of heterogeneous lithiated volumes with different kinetics. This observation evidences that different lithiation mechanisms can be recorded depending on the X-ray dose absorbed.

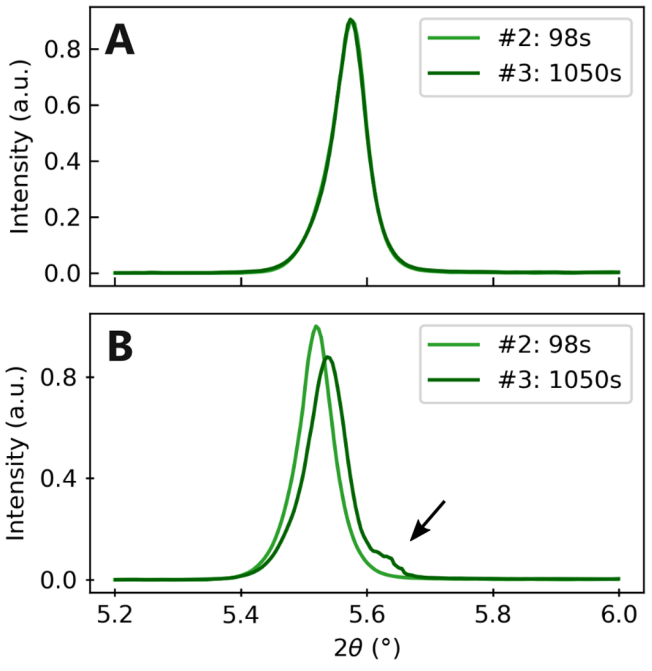


**Figure 4. 003 peak of NMC811 at locations #2 and #3 (A) at the initial state and (B) after charging for 3 h at C/8. The arrow points to a new peak.**

We can estimate the dose in material $i$ (NMC, electrolyte, or graphite) using the following approximation (see derivation in SI-6, Figure S5 and the corresponding simulation code in SI-10):

$$D_i = \frac{\alpha_i E e}{m_i} \tag{1}$$

with $\alpha_i$ being the absorbed photon flux ($s^{-1}$), calculated by propagating the incident photon flux across the different materials upstream, $E$ the photon energy (J), $e$ the accumulated exposure time (s), and $m_i$ the mass of material $i$ (cf. Table S1). The pouch bag, silicon window, and current collectors are considered in our calculations. Note that in all the experiments, care was taken to mount the pouch cell such that the anode was always upstream of the X-ray beam. After 3 h of charge at C/8, i.e. state of charge (SOC) 37.5%, at the highly irradiated location, the NMC material has received an X-ray dose of 11 MGy and the electrode is already damaged, as shown in Figure 4B. The NMC at location #2 received 1.8 MGy at SOC 56% when the X-ray beam effect can be seen (Figure 3D). At location #1 used as reference, the NMC received 79 kGy at the end of charge. In comparison, Blondeau et al.[16] reported a beam effect in an InSb electrode during X-ray absorption spectroscopy measurements with an estimated dose of 1−10 MGy, which is consistent with our observation of a significant effect on the most irradiated location where the dose is larger. Furthermore, Ortiz et al.[25] observed electrolyte decomposition from a dose of 20 kGy by radiolysis. In our experiment, the dose absorbed by the electrolyte at the reference location #1 is less than 5 kGy, which is also consistent with that report. Beam effects in the graphite electrode appear later when comparing location #3 and location #2. This is most likely due to the lower absorption coefficient of graphite that lowers the dose received for a given exposure, compared to the NMC (eq 1). Interestingly, the dose received by the graphite at location #3 at SOC 100% is about 1.1 MGy, which is consistent with the value of ∼1.8 MGy for the first visible beam effect in the NMC (see Tables S2 and S3). In light of these results, it is possible to propose a dose scale for beam damage: (1) no damages recorded below 80 kGy, (2) a modification of the apparent microstructure from about 1 to 4 MGy, and (3) a clear kinetics limitation from 11 MGy. This scale seems to fit for both NMC and graphite behavior and may be shared with other materials. The dose thresholds defined here set approximate limits where *operando* experiments can be safely performed on liquid Li-ion batteries, depending on the scientific purpose. If the microstructure is probed, a dose below 80 kGy is recommended, but it can reach about 4 MGy if only the lithiation mechanism is probed. The universal character of this dose scale is probably warranted by the fact that the origin of the beam damage is most likely not directly in the absorbing material, but rather in the surrounding organic compounds, as discussed in the following. Further measurements using different materials could further support this hypothesis but are out of the scope of this work.

Before discussing the internal origin of the beam damage and beyond the simple dose metric, we also anticipate the dose rate to be a key parameter of beam damage. While the dose is defined as the amount of radiative energy absorbed per unit mass, the dose rate is defined as the dose increment per unit time. Experiment 3 was performed to evidence dose rate effects, where pouch cell c at location #3 (PCc#3) of the


https://doi.org/10.1021/acsenergylett.3c00815
ACS Energy Lett. 2023, 8, 3323−3329

previous experiment is compared to another similar NMC811 pouch cell (PCd) probed on a single location with a different dose and dose rate. The several discontinuous 003 peak shifts of NMC811 in PCd (Figure S9), typical of successive phase transitions, were more pronounced than in PCc#3. Thus, the damages observed in PCd are more severe than in PCc#3, even though its dose is lower than for PCc#3 (Figure S12). Two different experimental conditions could explain the more severe damages observed in PCd (cf. Figures S10 and S11). It could be either due to the higher averaged and local (43% and 22% respectively) dose rate experienced by PCd, or it could be related to the measurement protocol of PCc#3 which includes intermittent beam exposure breaks. Those irradiation breaks could leave enough time to the electrode to heal, in agreement with results of Lim et al.,[26] who reported that they can limit the interaction with the binder using intermittent X-ray measurements. This shows that both dose rate and dose should be considered in beam damage.

The exact nature of the beam−battery interaction is still unclear, but it is likely related to the photoelectrons generated by beam absorption that dominates in the soft-to-hard X-ray range. Indeed, recent reports[27] suggest that the X-ray beam creates an electron cascade induced by the absorption. In short, the incoming X-ray beam produces photoelectrons while going through the material. These electrons propagate randomly around the absorption site and can still have enough energy to interact and create a cascade of secondary electrons of lower energy. The series of these secondary electrons indirectly induced can hence stretch to the micrometer scale and interact with the material environment via a broad range of energies. The cascade extent ensues from the material of higher absorption coefficient in the system. It interacts with either the absorbing material[28] or its environment (electrolyte, binder, etc.) and can result in an increase of resistivity, and finally kinetics hindrance as observed in this work and elsewhere.[15,16,29] In our case, the active material absorbs the radiation and transfers the photoelectrons to cause degradations into the surrounding environment. Since direct beam absorption in an electrolyte has been recently reported[25] to cause degradation, it is expected that the electron cascade could induce electrolyte aging with modified ion transfer properties. This decomposition could produce gas bubbles, though we did not manage to observe such a phenomenon in our experiments (Figure S16). If the direct beam absorption from electrolyte or binder was the cause of the degradation, the same damages should take place in both electrodes. However, we observe a small change in the anode only at the end of the charge, that is later than in the cathode. This matches well with the cascade mechanism mainly taking place in the electrode having the higher electronic density. The modification of Ni/Li antisite default rate and the temperature increase are evaluated, but those do not seem to prevail (Figures S13−S15 and Figure S17[27]). Other possible damages are stemming from the carbon-binder matrix, as Lim et al. recently showed that the latter can swell and dislocate, thus possibly isolating active particles.[26] The mechanical stability of the particle network guaranteed by the polyvinylidene fluoride (PVDF) can also be affected. Inded, in other fields, the beam-induced damages of PVDF are known and used to synthesize carbyne, for example.[30−32] The graphite absorption being weak, it explains why PVDF or electrolyte in the NMC electrode is damaged whereas it is not, or occurs later, in the graphite electrode. Cross-linking, crystallization, and production of radicals are some of the many possibilities of beam-induced electrolyte aging.[27,33,34] From this perspective, the chosen X-ray technique does not matter in the extent of damages, but its sensitivity may affect the onset dose value from which the degradations are visible.

In conclusion, different levels of X-ray-induced degradation can be identified, from material failure to almost indistinguishable effects. In the most obvious cases, large X-ray doses (typically above $10^1$ MGy in NMC) can result in an electrode material that appears inactive, undergoing a delayed charging or even an induced artificial phase transition. When the dose is lower (on the order of $10^0$ MGy), the peak positions are not altered but their intensity and width are modified, preventing further isotropic strain analysis and precise crystal structure refinements. This beam damage dose scale is shared between NMC and graphite and thus probably other materials. Additionally, we infer that the dose is not the only criterion defining the safe region to operate a battery since at a fixed dose; the increase of dose rate worsens damages. Our results finally incite limiting the dose below a threshold that keeps unbiased the phenomenon under probing, while using intermittent exposure or moderate X-ray flux to lower the dose rate.

The true nature of the beam damage is still evasive, and it is very likely that it has multiple origins. We introduced different possible beam damage mechanisms based on an electron cascade hindering kinetics, figured by a broadening of lithiation states whose extents depend on the dose or dose rate received. We underline that the beam damage is reported here for at least two different positive electrode materials and one negative electrode material and thus it is likely to be occurring in many battery materials. This work highlights that beam damage can also develop in a more insidious manner and yield subtle modifications of crystallographic features, therefore calling for reproducing measurements using systematic dose and dose-rate metrics. In their absence, the in-depth understanding of structural changes, as found in battery materials after given numbers of cycles, might contain unacceptable margins of error.

## ■ ASSOCIATED CONTENT

### Supporting Information

The Supporting Information and usefull notebook are available free of charge: The Supporting Information is available free of charge at https://pubs.acs.org/doi/10.1021/acsenergylett.3c00815.

Materials and methods, experimental precisions, full refined data set, theoretical evolution of 113 Bragg reflection intensity of NMC811, color maps and potential curves, dose estimation, graphite analysis, NMC811 under a higher dose rate, dose rate and beam shape considerations, dose calculations and Python module to calculate dose and transmission, Ni/Li antisite default effect, changes in transmission, and temperature increase (PDF)

## ■ AUTHOR INFORMATION

### Corresponding Author

**Samuel Tardif** − *Univ. Grenoble Alpes, CEA, IRIG, F-38000 Grenoble, France;* orcid.org/0000-0002-1786-8581; Email: samuel.tardif@cea.fr



https://doi.org/10.1021/acsenergylett.3c00815
ACS Energy Lett. 2023, 8, 3323−3329

## Authors

**Thibaut Jousseaume** − *Univ. Grenoble Alpes, CEA, IRIG, F-38000 Grenoble, France;* orcid.org/0000-0002-7547-6439

**Jean-François Colin** − *Univ. Grenoble Alpes, CEA, LITEN, F-38000 Grenoble, France*

**Marion Chandesris** − *Univ. Grenoble Alpes, CEA, LITEN, F-38000 Grenoble, France;* orcid.org/0000-0001-9936-635X

**Sandrine Lyonnard** − *Univ. Grenoble Alpes, CEA, IRIG, F-38000 Grenoble, France;* orcid.org/0000-0003-2580-8439

Complete contact information is available at: https://pubs.acs.org/10.1021/acsenergylett.3c00815


## Notes

The authors declare no competing financial interest.

## ■ ACKNOWLEDGMENTS

The "CEA Battery FOCUS" program is acknowledged for the funding of the PhD program of T.J. Beamtime at the ESRF was granted within the Battery Pilot Hub MA4929 "Multi-scale Multi-techniques investigations of Li-ion batteries: towards a European Battery Hub" and proposals IH-CH-1525 and IH-CH-1577. Funding from French ANR PIA3 Equipex+ project MAGNIFIX under grant agreement ANR-21-ESRE-0011 and ANR PEPR PIA4 project DIADEM-ESRF under grant agreement 22-PEXD-0011 are acknowledged, as well EU H2020 Research and Innovation Program project BIG-MAP under grant agreement No. 957189. Olivier Ulrich, Jean-Sébastien Micha, and Olivier Geaymond (BM32 beamline staff) are thanked for their help in the preparation of the experiments. Morgane Herbomel and Yvan Reynier are thanked for the manufacturing of electrodes, and Daniel Tomasi is thanked for the preparation of the pouch cells at CEA-LITEN.

## ■ REFERENCES


(1) Berhaut, C. L.; Dominguez, D. Z.; Kumar, P.; Jouneau, P.-H.; Porcher, W.; Aradilla, D.; Tardif, S.; Pouget, S.; Lyonnard, S. Multiscale Multiphase Lithiation and Delithiation Mechanisms in a Composite Electrode Unraveled by Simultaneous Operando Small-Angle and Wide-Angle X-Ray Scattering. *ACS Nano* **2019**, *13*, 11538−11551. PMID: 31560519.

(2) Tardif, S.; Dufour, N.; Colin, J.-F.; Gébel, G.; Burghammer, M.; Johannes, A.; Lyonnard, S.; Chandesris, M. Combining operando X-ray experiments and modelling to understand the heterogeneous lithiation of graphite electrodes. *J. Mater. Chem. A* **2021**, *9*, 4281−4290.

(3) Boulet-Roblin, L.; Sheptyakov, D.; Borel, P.; Tessier, C.; Novák, P.; Villevieille, C. Crystal structure evolution via operando neutron diffraction during long-term cycling of a customized 5 V full Li-ion cylindrical cell LiNi0.5Mn1.5O4 vs. graphite. *J. Mater. Chem. A* **2017**, *5*, 25574−25582.

(4) Darwiche, A.; Murgia, F.; Fehse, M.; Mahmoud, A.; Iadecola, A.; Belin, S.; La Fontaine, C.; Briois, V.; Hermann, R. P.; Fraisse, B.; Berthelot, R.; Sougrati, M. T.; Monconduit, L.; Stievano, L. Operando X-ray absorption spectroscopy applied to battery materials at ICGM: The challenging case of BiSb's sodiation. *Energy Storage Mater.* **2019**, *21*, 1−13.

(5) Swallow, J. E. N.; Fraser, M. W.; Kneusels, N.-J. H.; Charlton, J. F.; Sole, C. G.; Phelan, C. M. E.; Björklund, E.; Bencok, P.; Escudero, C.; Pérez-Dieste, V.; Grey, C. P.; Nicholls, R. J.; Weatherup, R. S. Revealing solid electrolyte interphase formation through interface-sensitive Operando X-ray absorption spectroscopy. *Nat. Commun.* **2022**, *13*, 6070.

(6) Schweidler, S.; Dreyer, S. L.; Breitung, B.; Brezesinski, T. Operando acoustic emission monitoring of degradation processes in lithium-ion batteries with a high-entropy oxide anode. *Sci. Rep.* **2021**, *11*, 23381.

(7) Merryweather, A. J.; Jacquet, Q.; Emge, S. P.; Schnedermann, C.; Rao, A.; Grey, C. P. Operando monitoring of single-particle kinetic state-of-charge heterogeneities and cracking in high-rate Li-ion anodes. *Nat. Mater.* **2022**, *21*, 1306−1313.

(8) Märker, K.; Xu, C.; Grey, C. P. Operando NMR of NMC811/Graphite Lithium-Ion Batteries: Structure, Dynamics, and Lithium Metal Deposition. *J. Am. Chem. Soc.* **2020**, *142*, 17447−17456.

(9) Martis, V.; Nikitenko, S.; Sen, S.; Sankar, G.; van Beek, W.; Filinchuk, Y.; Snigireva, I.; Bras, W. Effects of X-rays on Crystal Nucleation in Lithium Disilicate. *Cryst. Growth Des.* **2011**, *11*, 2858−2865.

(10) Stanley, H. B.; Banerjee, D.; van Breemen, L.; Ciston, J.; Liebscher, C. H.; Martis, V.; Merino, D. H.; Longo, A.; Pattison, P.; Peters, G. W. M.; Portale, G.; Sen, S.; Bras, W. X-ray irradiation induced reduction and nanoclustering of lead in borosilicate glass. *CrystEngComm* **2014**, *16*, 9331−9339.

(11) Coughlan, H. D.; Darmanin, C.; Kirkwood, H. J.; Phillips, N. W.; Hoxley, D.; Clark, J. N.; Vine, D. J.; Hofmann, F.; Harder, R. J.; Maxey, E.; Abbey, B. Bragg coherent diffraction imaging and metrics for radiation damage in protein micro-crystallography. *J. Synchrotron Radiat.* **2017**, *24*, 83−94.

(12) de la Mora, E.; Coquelle, N.; Bury, C. S.; Rosenthal, M.; Holton, J. M.; Carmichael, I.; Garman, E. F.; Burghammer, M.; Colletier, J.-P.; Weik, M. Radiation damage and dose limits in serial synchrotron crystallography at cryo- and room temperatures. *Proc. Natl. Acad. Sci. U. S. A.* **2020**, *117*, 4142−4151.

(13) Hasegawa, K.; Yamashita, K.; Murai, T.; Nuemket, N.; Hirata, K.; Ueno, G.; Ago, H.; Nakatsu, T.; Kumasaka, T.; Yamamoto, M. Development of a dose-limiting data collection strategy for serial synchrotron rotation crystallography. *J. Synchrotron Radiat.* **2017**, *24*, 29−41.

(14) Li, M.; Liu, W.; Luo, D.; Chen, Z.; Amine, K.; Lu, J. Evidence of Morphological Change in Sulfur Cathodes upon Irradiation by Synchrotron X-rays. *ACS Energy Lett.* **2022**, *7*, 577−582.

(15) Borkiewicz, O. J.; Wiaderek, K. M.; Chupas, P. J.; Chapman, K. W. Best Practices for Operando Battery Experiments: Influences of X-ray Experiment Design on Observed Electrochemical Reactivity. *J. Phys. Chem. Lett.* **2015**, *6*, 2081−2085.

(16) Blondeau, L.; Surblé, S.; Foy, E.; Khodja, H.; Belin, S.; Gauthier, M. Are Operando Measurements of Rechargeable Batteries Always Reliable? An Example of Beam Effect with a Mg Battery. *Anal. Chem.* **2022**, *94*, 9683−9689.

(17) Christensen, C. K.; Karlsen, M. A.; Drejer, A. Ø.; Andersen, B. P.; Jakobsen, C. L.; Johansen, M.; Sørensen, D. R.; Kantor, I.; Jørgensen, M. R. V.; Ravnsbæk, D. B. Beam damage in operando X-ray diffraction studies of Li-ion batteries. *J. Synchrotron Radiat.* **2023**, *30*, 561−570.

(18) Schellenberger, M.; Golnak, R.; Quevedo Garzon, W.; Risse, S.; Seidel, R. Accessing the solid electrolyte interphase on silicon anodes for lithium-ion batteries in-situ through transmission soft X-ray absorption spectroscopy. *Mater. Today Adv.* **2022**, *14*, 100215.

(19) Nelson, J.; Yang, Y.; Misra, S.; Andrews, J. C.; Cui, Y.; Toney, M. F. Identifying and managing radiation damage during in situ transmission x-ray microscopy of Li-ion batteries. *Proceedings Volume 8851, X-Ray Nanoimaging: Instruments and Methods*, SPIE Optical Engineering + Applications, San Diego, CA, 2013.

(20) Märker, K.; Reeves, P. J.; Xu, C.; Griffith, K. J.; Grey, C. P. Evolution of structure and lithium dynamics in $LiNi_{0.8}Mn_{0.1}Co_{0.1}O_2$ (NMC811) cathodes during electrochemical cycling. *Chem. Mater.* **2019**, *31*, 2545−2554.

(21) Zheng, S.; Hong, C.; Guan, X.; Xiang, Y.; Liu, X.; Xu, G.-L.; Liu, R.; Zhong, G.; Zheng, F.; Li, Y.; Zhang, X.; Ren, Y.; Chen, Z.; Amine, K.; Yang, Y. Correlation between long range and local

structural changes in Ni-rich layered materials during charge and discharge process. *J. Power Sources* **2019**, *412*, 336−343.
(22) Park, J.; Zhao, H.; Kang, S. D.; Lim, K.; Chen, C.-C.; Yu, Y.-S.; Braatz, R. D.; Shapiro, D. A.; Hong, J.; Toney, M. F.; Bazant, M. Z.; Chueh, W. C. Fictitious phase separation in Li layered oxides driven by electro-autocatalysis. *Nat. Mater.* **2021**, *20*, 991−999.
(23) Nowack, L.; Grolimund, D.; Samson, V.; Marone, F.; Wood, V. Rapid Mapping of Lithiation Dynamics in Transition Metal Oxide Particles with Operando X-ray Absorption Spectroscopy. *Sci. Rep.* **2016**, *6*, 21479.
(24) Li, S.; Jiang, Z.; Han, J.; Xu, Z.; Wang, C.; Huang, H.; Yu, C.; Lee, S.-J.; Pianetta, P.; Ohldag, H.; Qiu, J.; Lee, J.-S.; Lin, F.; Zhao, K.; Liu, Y. Mutual modulation between surface chemistry and bulk microstructure within secondary particles of nickel-rich layered oxides. *Nat. Commun.* **2020**, *11*, 4433.
(25) Ortiz, D.; Steinmetz, V.; Durand, D.; Legand, S.; Dauvois, V.; Maître, P.; Le Caër, S. Radiolysis as a solution for accelerated ageing studies of electrolytes in Lithium-ion batteries. *Nat. Commun.* **2015**, *6*, 6950.
(26) Lim, C.; Kang, H.; De Andrade, V.; De Carlo, F.; Zhu, L. Hard X-ray-induced damage on carbon−binder matrix for *in situ* synchrotron transmission X-ray microscopy tomography of Li-ion batteries. *J. Synchrotron Radiat.* **2017**, *24*, 695−698.
(27) Bras, W.; Myles, D. A. A.; Felici, R. When x-rays alter the course of your experiments. *J. Phys.: Condens. Matter* **2021**, *33*, 423002.
(28) Thomä, S. L. J.; Zobel, M. Beam-induced redox chemistry in iron oxide nanoparticle dispersions at ESRF−EBS. *J. Synchrotron Radiat.* **2023**, *30*, 440−444.
(29) Bras, W.; Newton, M. A.; Myles, D. A. A.; Felici, R. High-intensity X-ray beams can influence the kinetics in a time-resolved experiment. *Nat. Rev. Methods Primers* **2022**, *2*, 22.
(30) Brzhezinskaya, M.; Zhivulin, V. E. Controlled modification of polyvinylidene fluoride as a way for carbyne synthesis. *Polym. Degrad. Stab.* **2022**, *203*, 110054.
(31) Duca, M. D.; Plosceanu, C. L.; Pop, T. Effect of X-rays on poly(vinylidene fluoride) in X-ray photoelectron spectroscopy. *J. Appl. Polym. Sci.* **1998**, *67*, 2125−2129.
(32) Pesin, L.; Morilova, V.; Zherebtsov, D.; Evsyukov, S. Kinetics of PVDF film degradation under electron bombardment. *Polym. Degrad. Stab.* **2013**, *98*, 666−670.
(33) Susich, G.; King, A. O.; Dogliotti, L. M. Radiation-Induced Crystallization of Sucrose. *Science* **1959**, *130*, 567−568.
(34) Steinrück, H.-G.; Cao, C.; Lukatskaya, M. R.; Takacs, C. J.; Wan, G.; Mackanic, D. G.; Tsao, Y.; Zhao, J.; Helms, B. A.; Xu, K.; Borodin, O.; Wishart, J. F.; Toney, M. F. Interfacial Speciation Determines Interfacial Chemistry: X-ray-Induced Lithium Fluoride Formation from Water-in-salt Electrolytes on Solid Surfaces. *Angew. Chem. - Int. Ed.* **2020**, *59*, 23180−23187.


https://doi.org/10.1021/acsenergylett.3c00815
*ACS Energy Lett.* 2023, 8, 3323−3329